



ELSEVIER

Contents lists available at SciVerse ScienceDirect

Journal of Sound and Vibration

journal homepage: www.elsevier.com/locate/jsv

Modeling and identification of frictional forces at a contact interface experiencing micro-vibro-impacts

Fatemeh Pourahmadian^a, Hamid Ahmadian^{a,*}, Hassan Jalali^b

^a Center of Excellence in Experimental Solid Mechanics and Dynamics, Iran University of Science and Technology, Narmak, Tehran 16848, Iran

^b Department of Mechanical Engineering, Arak University of Technology, Arak 38135-1177, Iran

ARTICLE INFO

Article history:

Received 22 September 2010

Received in revised form

13 January 2012

Accepted 26 January 2012

Handling Editor: L.N. Virgin

ABSTRACT

Modeling and identification of restoring forces at contact interfaces is an inevitable part of investigating the dynamic characteristics of mechanical systems. As the vibration amplitude increases, various nonlinear mechanisms such as micro/macro-slip and micro-impacts activate in the interface. This paper considers the nonlinear behavior of a frictional contact in situations where micro-impacts develop in the normal direction to the friction surface. It investigates the effect of variable normal load on the contact frictional forces, and defines a friction model capable of taking into account this effect. In an experimental case study, the contact is excited using a dual sine force to allow a reliable dual-mode identification procedure. The measured data and the normal modes of the corresponding linear system are employed to define the system nonlinear modes used to expand the system response. This provides a reduced order model containing dominant nonlinear effects in the contact interface. Force state mapping method is employed to identify the contact restoring forces. The experimentally obtained forces are employed to determine the parameters of a new friction law defined by modifying the Valanis model. It is shown the model is capable of predicting the main nonlinear characteristics of the contact interface and regenerates the experimental results at different vibration response levels.

© 2012 Elsevier Ltd. All rights reserved.

1. Introduction

Accurate predictions of a structure dynamics require precise modeling of its linear and nonlinear behavior. Joints and connections are common elements of mechanical systems, and modeling their contact interfaces, which involve complicated nonlinear phenomena, is an inevitable part of structural analysis. Surface roughness and normal preload have a significant influence on the contact nonlinear properties which in turn play a key role in the dynamic behavior of the system at different vibration amplitudes; at low response levels, the interface is in the stick regime and the system behaves linearly. As the vibration amplitude increases, micro/macro-slip develops in the tangential direction of the contact interface. At the same time in the normal direction of the contact interface vibro-impacts may be activated depending on the surface roughness and the normal preload. An accurate contact model must include all these nonlinear characteristics involved in the contact interface.

Literature on contact dynamics can be classified into three categories. The first group investigates the friction phenomenon and considers the normal preload to be constant [1–8]. The second group focuses on impact dynamics and

* Corresponding author. Tel.: +98 21 77240198; fax: +98 21 77240488.

E-mail address: ahmadian@iust.ac.ir (H. Ahmadian).

assumes a frictionless contact [9–11]. The contact tangential friction force is strongly affected by the variation of the contact normal force. Nevertheless, the number of studies in the third group which investigates this interaction and considers the contact as a whole is limited [12–15].

Friction phenomenon is an old, but still active and important, research topic. Studies of Den Hartog [16], Dowell [17] and Ferri [18] paved the way for the others in this field. Berger [19] provided a comprehensive account of the various mechanisms involved in the contact interface. There are various friction models which mathematically describe the experimentally observed behavior of the friction force [1–6]. They are remarkably insightful in terms of understanding the nonlinear characteristics of the friction phenomenon. A comprehensive overview on a range of constitutive models for joint interfaces is provided by Gaul and Nitsche [20].

The dynamics of vibro-impact is highly complicated. Surface roughness has a considerable effect on the dynamical behavior of the contact in the normal direction. Assuming a distribution for the height of contact surfaces asperities, various models were developed based on the Hertzian theory [21]. These models demonstrate the nonlinear nature of the contact normal stiffness, while the normal damping mechanisms are usually disregarded. A commonly used model which describes the impact energy dissipation by a nonlinear term was proposed by Hunt and Crossley [10]. Zhang and Sharf [11] carried out a set of experiments in order to validate the Hunt–Crossley type of contact force models. Comparing the experimental results to the model predictions showed that these models are not capable of capturing the complicated damping mechanisms such as plastic deformations in the normal direction.

In an interface experiencing both impact and friction, the contact normal and tangential restoring force may not be considered separately due to their strong interactions. There are a number of 3D models considering the contact as a whole but none of them is capable of representing all the observed mechanisms in the contact interface. The model proposed by Han and Gilmore [12] accounts for the normal–tangential interactions using the static and kinetic coefficients of friction. Tenaglia et al. [13] and Gonthier et al. [14] introduced two different 3D contact models taking into account the micro- and macro-slippage effects. However, the effect of the normal force on the contact shear stiffness in these models is ignored. Gaul and Mayer [15] developed an improved approach to model contact interfaces of joints in finite element analysis. A study on elasticity of the contacting bodies which accompanies a full description of a three dimensional point contact model is provided in [21]. A comprehensive literature survey on contact dynamics is performed by Gilardi and Sharf [22].

The current article is a continuation of authors' previous work [23], where the dynamical behavior of a fixed-frictionally supported beam at different vibration amplitudes is investigated. In their test set up a relatively high normal preload was exerted on the contact allowing a constant normal load to be assumed on the interface and no presence of micro-impacts. In [23] Nonlinear Normal Modes (NNMs) of the test structure were obtained from experimental data and later used in the identification procedure of the contact frictional forces.

By decreasing the contact normal preload, in the present study, the investigation is extended to the situations where micro-impacts as well as micro/macro-slip are present in the contact interface. A dual-mode test procedure for nonlinear systems [24] is employed and by identifying NNMs from experimental data, a multimode analysis of the system is performed [25]. These provide the basis for a multimode identification procedure and leads to identifying the two components of the contact restoring forces simultaneously. A new friction law based on the Valanis model is introduced to account the micro/macro-slip, as well as to capture the effect of the normal–tangential interactions. The model parameters are identified by minimizing the difference between measured test data and the analytical predictions using the Genetic Algorithm. The model predictions show a good agreement with the experimentally obtained results.

The remainder of the paper is structured as follows. Section 2 describes the continuous model formulation of the structure under consideration and a reduced-order model of the system suitable for the identification procedure is obtained. The experimental set-up and the test procedure are presented in Section 3. The recorded experimental data and the normal modes of the corresponding linear system are employed in Section 4 to identify the system nonlinear modes. The nonlinear normal modes are used in the identification of contact parameters. In Section 5, the new friction model is introduced and its parameters are identified. The proposed model is validated in this section by comparing the experimental results and the model predictions.

2. Mathematical modeling

This study investigates the friction force between the two contacting surfaces experiencing micro-vibro-impacts. The contact interface shown in Fig. 1 forms the boundary of a fixed-frictionally supported beam. The system consists of a continuous beam and a mass block hanging from the beam end by a string. The normal preload at the contact interface, provided by the suspended mass block, is chosen such that, as the vibration amplitude increases, micro-impacts in the

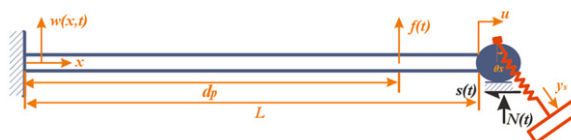


Fig. 1. A slender beam with frictional contact boundary support.

normal direction as well as micro/macro-slip in the tangential direction are activated. The two components of contact restoring force are considered as unknowns in the mathematical model of the system.

The dynamic behavior of the beam is modeled using the Euler–Bernoulli beam theory with a modulus of elasticity of E , mass density of ρ , cross sectional area of A , cross sectional moment of inertia of I , and length of L . The frequency range in which the dynamic behavior of the structure is investigated is well away from the resonance frequency corresponding to the first axial mode of the beam; hence, the effect of axial inertia is neglected and the beam is modeled as a spring of stiffness $k_b=EA/L$ in the axial direction. The frictional contact support is provided by a pin which is welded to the beam end and slips on a steel block surface as shown in Fig. 1. The pin has a radius of r , mass of m_p , and mass moment of inertia of J_p . The hanging mass block is modeled as a spring pendulum suspended from the beam end. The block has a total mass of m_s and mass moment of inertia of J_s and the string has a length of l_s and an axial stiffness of k_s . The structure is excited using a concentrated force $f(t)$ at the distance d_p measured from its fixed end.

The governing equations of the system reported in the followings are obtained using the extended Hamilton’s principle and its details are carried out in Appendix A. The beam lateral motion $w(x,t)$ is governed by the Euler–Bernoulli beam theory:

$$EI \frac{\partial^4 w}{\partial x^4} - k_b u(t) \frac{\partial^2 w}{\partial x^2} + \rho A \frac{\partial^2 w}{\partial t^2} = f(t) \delta(x-d_p). \quad (1)$$

The second term in the left-hand side of Eq. (1) accounts for the effect of the axial force on the beam lateral vibrations and u is the beam tip axial movement.

The beam tip axial deformation causes a relative displacement at the contact interface and applies a base excitation to the suspended mass block. The governing equation of the beam tip axial deformation, $u(t)$ is

$$m_s \left(\ddot{\xi} - 2r \frac{\partial \ddot{w}(L,t)}{\partial x} + l_s \ddot{\theta}_s \right) + k_b u(t) + S(t) = 0, \quad (2)$$

where $\xi(t)$ is the relative tangential displacement at the contact interface, $S(t)$ is the contact interface friction force, and θ_s is the rotational displacement of the spring as shown in Fig. (1). The spring pendulum equations of motion is described as

$$m_s (\ddot{\eta}(t) - \ddot{y}_s) - k_s y_s = 0, \quad (3)$$

$$J_s \ddot{\theta}_s + m_s l_s \left(\ddot{\xi} - 2r \frac{\partial \ddot{w}(L,t)}{\partial x} + l_s \ddot{\theta}_s \right) + m_s g l_s \theta_s = 0, \quad (4)$$

where y_s is the stretch in the spring k_s , from its static equilibrium position.

The boundary conditions at the beam fixed end are

$$w(0,t) = 0, \quad \frac{\partial w(0,t)}{\partial x} = 0. \quad (5)$$

The equilibrium of the shear forces and the bending moments at the frictional support are

$$EI \frac{\partial^3 w(L,t)}{\partial x^3} - k_b u(t) \frac{\partial w(L,t)}{\partial x} - m_p \ddot{\eta}(t) - m_s (\ddot{\eta}(t) - \ddot{y}_s) + N(t) = 0, \quad (6)$$

$$EI \frac{\partial^2 w(L,t)}{\partial x^2} + r EI \frac{\partial^3 w(L,t)}{\partial x^3} + r S(t) \left(1 + \frac{\partial w(L,t)}{\partial x} \right) + J_p \frac{\partial \ddot{w}(L,t)}{\partial x} - r m_s \left(\ddot{\xi} - 2r \frac{\partial \ddot{w}(L,t)}{\partial x} + l_s \ddot{\theta}_s \right) \left(1 - \frac{\partial w(L,t)}{\partial x} \right) = 0, \quad (7)$$

where $N(t)$ stands for the contact normal force and $\eta(t)$ indicates the relative normal displacement at the contact interface. Relative normal displacement at the contact interface, $\eta(t)$, is governed by the lateral deflection and rotation of the beam end, due to offset r , i.e.

$$\eta(t) = w(L,t) + r \frac{\partial w(L,t)}{\partial x}. \quad (8)$$

Also the relative tangential displacement at the contact interface, $\xi(t)$, is governed by three different effects as

$$\xi(t) = -\frac{1}{2} \int_0^L \left(\frac{\partial w(x,t)}{\partial x} \right)^2 dx + r \frac{\partial w(L,t)}{\partial x} + u(t). \quad (9)$$

The first term in the right-hand side of Eq. (9) stands for the beam shortening effect due to its lateral vibration, the second term shows the relative displacement due to the rotation of the beam end, and the last term indicates axial deformation of the beam. The structure under consideration does not experience large deformation, however considering all mechanisms that affect the relative tangential displacement in Eq. (9), including the beam shortening effect, allows more accurate hysteresis loops to be obtained, and subsequently a more precise identification procedure to be applied.

The objective is to identify the two unknown components of the contact restoring forces, $S(t)$ and $N(t)$, using experimental measurements. A reduced order model of the system along with the recorded test data provide the elements needed to apply a multimode identification of $S(t)$ and $N(t)$ simultaneously, using the force state mapping method [26,27].

The Galerkin method is a common approach in model order reduction. In Ref. [23], it is shown employing nonlinear modes as the Galerkin trial functions allows the behavior of system to be expressed accurately using a small number of

coordinates and leads to precise identification of unknown parameters. In the present study, the system response is expanded using nonlinear modes as

$$\begin{Bmatrix} w(x,t) \\ u(t) \\ y_s(t) \\ \theta_s(t) \end{Bmatrix} = \sum_{i=1}^n \begin{Bmatrix} \tilde{\varphi}_i(x) \\ \tilde{u}_i \\ \tilde{y}_{si} \\ \tilde{\theta}_{si} \end{Bmatrix} q_i(t), \quad (10)$$

where $q_i(t)$, $i=1,2,\dots,n$, are generalized coordinates, and $\{\tilde{\varphi}_i(x), \tilde{u}_i, \tilde{y}_{si}, \tilde{\theta}_{si}\}^T$ are n independent real valued nonlinear modes of the structure. These modes are obtained later in Section 4 from experimental data. The expansion series described in Eq. (10) is substituted into the nonlinear equations of motion (1)–(4) and their projection on each individual nonlinear mode is set to zero

$$\int_0^L \tilde{\varphi}_i(x) \left(EI \frac{\partial^4 w}{\partial x^4} - k_b u \frac{\partial^2 w}{\partial x^2} + \rho A \frac{\partial^2 w}{\partial t^2} - f(t) \delta(x-d_p) \right) dx + \tilde{u}_i \left(m_s \left(\ddot{\xi} - 2r \frac{\partial \ddot{w}(L,t)}{\partial x} + l_s \ddot{\theta}_s \right) + k_b u + S(t) \right) + \tilde{\theta}_{si} \left(J_s \ddot{\theta}_s + m_s l_s \left(\ddot{\xi} - 2r \frac{\partial \ddot{w}(L,t)}{\partial x} + l_s \ddot{\theta}_s \right) + m_s g l_s \theta_s \right) + \tilde{y}_{si} (m_s (\ddot{\eta}(t) - \ddot{y}_s) - k_s y_s) = 0, \quad i = 1, 2, \dots, n. \quad (11)$$

Using integration by parts twice, the effects of boundary conditions (5)–(7) appear in the obtained discrete model. This leads to n discrete equations viewed in matrix notation as

$$[M]\{\ddot{q}\} + [K]\{q\} + \{F_c\} = \{F_{ext}\}, \quad (12)$$

where $[M]$ and $[K]$ are the generalized mass and stiffness matrices, $\{F_c\}$ is the generalized restoring forces at the contact interface and $\{F_{ext}\}$ is the generalized excitation force vector. The matrices $[M]$ and $[K]$ are known and the vectors $\{F_{ext}\}$ and $\{\ddot{q}\}$ are reconstructed from the measured force and accelerations. Hence, all the terms in Eq. (12), except for $\{F_c\}$ which contains the contact forces $S(t)$ and $N(t)$, are known. One may employ force state mapping technique [26,27] to identify relations between the contact forces $S(t)$ and $N(t)$ and the support relative displacements and velocities in the corresponding directions.

In the followings, experiments on the structure shown in Fig. 1 are reported and information required to identify the nonlinear mode shapes of the contact restoring force components are obtained.

3. Experimental case study

A steel beam of length $L=600$ mm, width $b=40$ mm and thickness $h=5$ mm clamped at one end and constrained by a frictional support at the other end is employed was this experimental study. A steel pin of radius $r=6$ mm with the length equal to the beam width was welded to the end of the beam and slides on a steel block; this provides a line contact at the frictional support. A normal preload was applied to the contact interface using the suspended mass block, of 7 kg, as shown in Fig. 2.

The main goal in this work is to study the slip and vibro-impact mechanisms at a frictional contact interface and their coupling effects. The test setup is designed to simultaneously excite and measure these two effects developing in two perpendicular directions. Using a simple experimental setup – for example an isolated contact interface – has the difficulty in exciting these two mechanisms simultaneously and two shakers must be used for simultaneously exciting the slip and

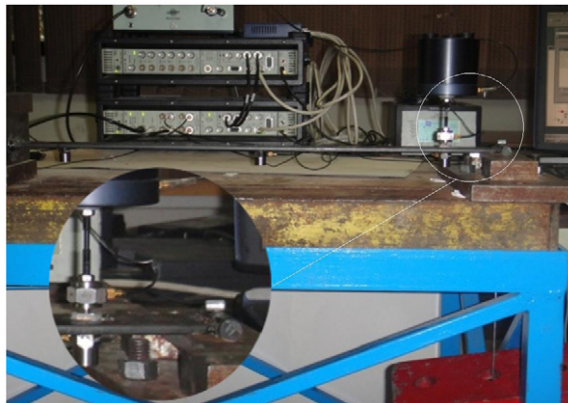


Fig. 2. The test set-up of frictionally supported beam.

impact mechanisms. Using an elastic beam in the test setup makes it possible to excite the nonlinear contact mechanisms in two perpendicular directions using one force exciter.

The structure was excited using a B&K4200 mini shaker attached through a stinger to the beam at distance $d_p=550$ mm from the clamped end. A B&K8200 force transducer was placed between the stinger and the structure to measure the excitation force, $f(t)$. Three accelerometers were mounted on the beam at $x_1=550$ mm, $x_2=300$ mm and $x_3=50$ mm, measured from the beam fixed end.

A dual-sine force was applied to the structure such that the system response was dominated by two modes. This allowed a reliable multimode identification procedure to be applied and consequently, the two components of the contact restoring force were obtained. Nonlinear mechanisms at the contact interface become activated in high vibration amplitudes. The structure was excited in the vicinity of its first and second resonance frequencies, so that the system could experience very high response levels without requiring high levels of excitation.

Applying a multi-harmonic excitation to a nonlinear system requires some considerations as the nonlinearity generates higher-order harmonics in the system response. Furthermore, in both experimental and identification procedures Fourier expansions of the measured time signals are required. And unless the two exciting frequencies are commensurable, leakage may lead to erroneous force identification results. Exciting the system by two commensurable frequencies near to the first and second natural frequencies of the structure requires modification of the corresponding linear system. In the structure model the transducers were considered as added masses. The transducer arrangement affects the natural frequencies of the system therefore the positions of the force and acceleration transducers were determined such that the first and second resonance frequencies of the corresponding linear system became nearly commensurable. This modification resolved the leakage problem, and allowed a simple definition for the nonlinear mode shapes. The nonlinear mode shapes make it possible to express the system response by a small number of coordinates.

It should be mentioned the transducers mass effects are not shown in Eq. (1) to keep the problem statement simple. They are taken into consideration in the mathematical model of the system, by dividing the beam model into four parts. The first section spans between the fixed end and the accelerometer three at x_3 , parts two and three are located between the three accelerometers, and part four is located between driving point and the frictional support. In deriving the compatibility equations between each two parts, it is assumed that the displacements and slopes are continuous but the shear forces and bending moments abruptly change due to mass and inertia effects of the transducers.

Initially, the structure was excited using a low level random force, ensuring of the linear behavior of the system, and the linear frequency response functions were measured. The linearity check was performed by observing the coherence function to be close to unity. It is worth mentioning in FRF measurement the coherence function is always checked to make sure the force–response relations are linear and measured signals are not corrupted with noise.

Fig. 3 shows the measured frequency response function at the driving point. The natural frequencies of the corresponding linear system are tabulated in Table 1. It shows the second natural frequency is approximately three times as much as the first natural frequency.

In the next step, the dynamic behavior of the structure was recorded while nonlinear mechanisms were developed in the contact interface. The experiments were conducted in three different response levels. In each level, the structure is excited, using a dual sine force, such that the system response contains certain characteristics. The excitation signal has five parameters; two amplitudes, two frequencies and phase shifts between the harmonics. At each response level, the exciting force harmonics were set close to the fundamental and second resonant frequencies of the corresponding linear system, and their ratio was 1:3. In the conducted experiments, there was no phase shift between the two excitation harmonics. In loading case, the force signal amplitudes were tuned such that the amplitudes of the corresponding harmonics in auto spectrum of the driving point acceleration remained as specified in Table 2. This way significant contribution of both modes in the system response was guaranteed and a reliable dual-mode identification procedure was performed using the recorded data.

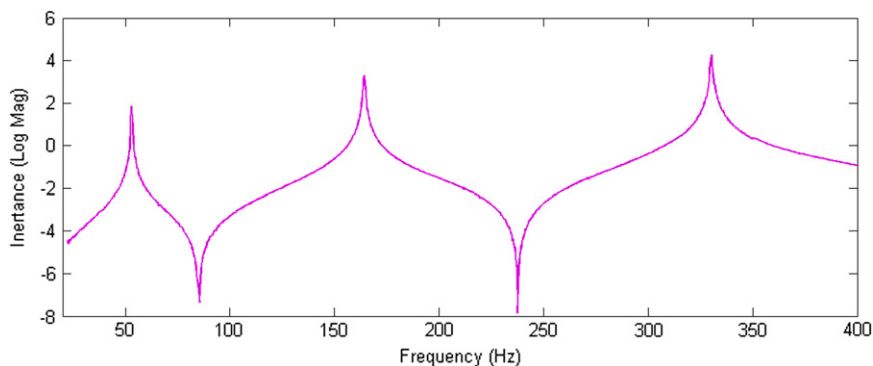


Fig. 3. Driving point frequency response at low level excitations.

Table 1
Resonance frequencies at low level random excitations (Hz).

ω_1	ω_2	ω_3
54.85	166.2	339.25

Table 2
The amplitudes of the acceleration signal harmonics at the deriving point.

Load case	A_1 (m/s ²)	A_2 (m/s ²)
1	14	34
2	17.5	42.5
3	20	50

Table 3
Identified parameters of the contact interface at stiction.

Parameter	k_t (N/m)	k_n (N/m)
Value	3.95e6	2.37e7

In the next section, the recorded test results and the mode shapes of the corresponding linear system are employed to construct the nonlinear modes used in Eq. (10).

4. Reconstructing the nonlinear mode shapes

The measured acceleration signals are used in this section to identify the nonlinear mode shapes used in the Galerkin projection, introduced in Eq. (11). The measured accelerations and obtained nonlinear modes are employed later to calculate the generalized coordinates using Eq. (10).

The system response contains two dominant harmonics near the first and second resonance frequencies of the structure, and the mode shapes of the corresponding linear system can be considered as close approximations of the nonlinear modes used in Eq. (10) to expand the system response and in Eq. (11) to accomplish the projection. A new approach for identifying NNMs is introduced by the authors in [25], which employs the mode shapes of the corresponding linear system and experimental data to obtain nonlinear modes. Following describes the corresponding linear system where its mode shapes are used to identify the nonlinear mode shapes.

One may obtain the equations of motion of the corresponding linear system by neglecting all the nonlinear terms in Eqs. (1)–(7). At low response levels the structure behaves linearly and the restoring forces in the contact interface is modeled using two linear springs, one in the normal and the other one in the tangential direction. Consequently the two components of the contact restoring force, $S(t)$ and $N(t)$, are described as

$$\begin{aligned} S(t) &= k_t \left(r \frac{\partial w(L,t)}{\partial x} + u(t) \right), \\ N(t) &= k_n \eta(t), \end{aligned} \quad (13)$$

where k_t and k_n are the tangential and normal stiffness of the contact interface, respectively. Now, the corresponding linear system is completely described. The characteristic equation of the linear system is formed, and using the measured natural frequencies tabulated in Table 1, the two parameters of the contact interface k_t and k_n are identified. The results are tabulated in Table 3.

Identification of the contact parameters at stiction enables one to evaluate the mode shapes of the corresponding linear system. Then, the structure response is expanded using the first m linear mode shapes as

$$\begin{Bmatrix} w(x,t) \\ u(t) \\ y_s(t) \\ \theta_s(t) \end{Bmatrix} = \sum_{i=1}^m \begin{Bmatrix} \varphi_i(x) \\ u_i \\ y_{si} \\ \theta_{si} \end{Bmatrix} p_i(t), \quad (14)$$

where $p_i(t)$ is the generalized coordinate and its coefficient vector is the corresponding linear mode shape. One may employ Eq. (14) to define a direct relationship between the measured accelerations and corresponding generalized

coordinates as

$$\ddot{\mathbf{p}}(t) = \begin{Bmatrix} \ddot{p}_1(t) \\ \ddot{p}_2(t) \\ \vdots \\ \ddot{p}_m(t) \end{Bmatrix} = \begin{bmatrix} \varphi_1(x_1) & \varphi_2(x_1) & \cdots & \varphi_m(x_1) \\ \varphi_1(x_2) & \varphi_2(x_2) & \cdots & \varphi_m(x_2) \\ \vdots & \vdots & \ddots & \vdots \\ \varphi_1(x_j) & \varphi_2(x_j) & \cdots & \varphi_m(x_j) \end{bmatrix}^+ \begin{Bmatrix} \ddot{w}(x_1,t) \\ \ddot{w}(x_2,t) \\ \vdots \\ \ddot{w}(x_j,t) \end{Bmatrix} = \Phi^+ \ddot{\mathbf{w}}, \quad \Phi^+ = (\Phi^T \Phi)^{-1} \Phi^T \quad (15)$$

Logically, the number of mode shapes used in Eq. (15) may not exceed the number of independently measured vibration signals, i.e. the generalized coordinate vector is determined using the measured accelerations at j points, where $j \geq m$. It is possible to estimate the number of mode shapes contributing in the dynamic response of the structure and subsequently, employ a sufficient number of accelerometers in the measurement setup.

The accelerometers were located on the beam therefore the discrete generalized coordinates, u_i , y_{si} and θ_{si} do not appear in the mode shape matrix of Eq. (15). Next, a Fourier series is fitted to every generalized acceleration signal as

$$\ddot{p}_i(t) = \sum_{k=1}^K A_{ki} \sin(k\omega t + \psi_{ki}), \quad i = 1, 2, \dots, m. \quad (16)$$

Coefficients A_{ki} and ψ_{ki} in the Fourier expansion are obtained from data fitting [28]. The generalized displacement $p_i(t)$ is obtained by performing time integrations of Eq. (16),

$$p_i(t) = - \sum_{k=1}^K \frac{A_{ki}}{(k\omega)^2} \sin(k\omega t + \psi_{ki}). \quad (17)$$

Substituting $p_i(t)$, obtained from Eq. (17), in Eq. (14), one obtains

$$\begin{Bmatrix} w(x,t) \\ u(t) \\ y_s(t) \\ \theta_s(t) \end{Bmatrix} = - \sum_{i=1}^m \begin{Bmatrix} \varphi_i(x) \\ u_i \\ y_{si} \\ \theta_{si} \end{Bmatrix} \sum_{k=1}^K \frac{A_{ki}}{(k\omega)^2} \sin(k\omega t + \psi_{ki}). \quad (18)$$

The recorded test data shows the system response is dominated by two harmonics, but more generalized coordinates are employed ($m=3$), in Eq. (18), in order to properly express the system response using linear mode shapes.

Szemplinska-Stupnicka [29,30] introduced a modification to single mode response predictions of nonlinear systems which makes it possible to accurately describe the nonlinear system response using the minimum number of generalized coordinates. Following Szemplinska-Stupnicka proposal, the authors introduced a method for identifying NNMs from test data [25] in which the system response is multi-harmonic, and the structure response is expanded by a few nonlinear modes. In this paper, the response of the system is approximated by two real-valued nonlinear modes as

$$\begin{Bmatrix} w(x,t) \\ u(t) \\ y_s(t) \\ \theta_s(t) \end{Bmatrix} = \begin{Bmatrix} \tilde{\varphi}_1(x) \\ \tilde{u}_1 \\ \tilde{y}_{s1} \\ \tilde{\theta}_{s1} \end{Bmatrix} a_1 \sin(\omega t + \psi_1) + \begin{Bmatrix} \tilde{\varphi}_3(x) \\ \tilde{u}_3 \\ \tilde{y}_{s3} \\ \tilde{\theta}_{s3} \end{Bmatrix} a_3 \sin(3\omega t + \psi_3). \quad (19)$$

Setting $K=2$ in Eq. (18) and equating the right hand sides of Eqs. (18) and (19), the nonlinear modes are obtained

$$\begin{Bmatrix} \tilde{\varphi}_j(x) \\ \tilde{u}_j \\ \tilde{y}_{sj} \\ \tilde{\theta}_{sj} \end{Bmatrix} = \frac{1}{\sqrt{A_{j1}^2 + A_{j2}^2 + \dots + A_{jm}^2}} \sum_{i=1}^m A_{ji} \begin{Bmatrix} \varphi_i(x) \\ u_i \\ y_{si} \\ \theta_{si} \end{Bmatrix}, \quad j = 1, 3. \quad (20)$$

The nonlinear mode shapes described in Eq. (19) are considered real provided that the phases of the terms corresponding to each frequency in Eq. (18) are (nearly) the same, otherwise the assumed nonlinear modes are complex. In the system under consideration, the maximum phase difference between the terms whose frequencies are identical in Eq. (18) is less than 10° , therefore the nonlinear modes are considered real-valued.

The number of mode shapes, m , in Eq. (18) is set to three, i.e. three linear mode shapes are used to define each nonlinear mode shape. The corresponding generalized coordinates of these three modes, $p_i(t)$, $i=1,2,3$, are shown in Fig. 4 when the amplitude of the first harmonic of the acceleration signal at the driving point is 20 m/s^2 and the amplitude of the second harmonic is 50 m/s^2 . In this case, the system experienced the largest amplitude of vibration in the conducted experiments, and the most deviations of the nonlinear modes from the corresponding linear mode shapes are expected. As it is seen in Fig. 4, the third linear mode has a marginal contribution in the nonlinear modes. Fig. 5 shows the system response at the driving point, reconstructed using the nonlinear modes obtained from Eq. (20), and compares it with the measured accelerations. There is an excellent agreement between the measured and predicted responses which reaffirms the choice of $m=3$ in constructing the nonlinear modes. It is worth mentioning in the Fourier series expansion of $\ddot{q}(t)$ only the first five terms are considered, and $q(t)$ is obtained through analytical integration.

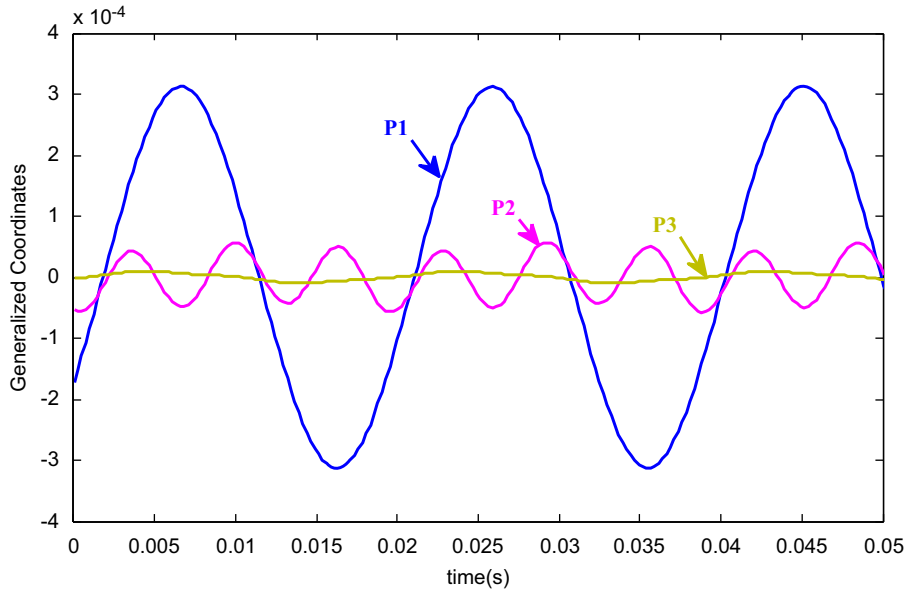


Fig. 4. The generalized coordinates vs. time.

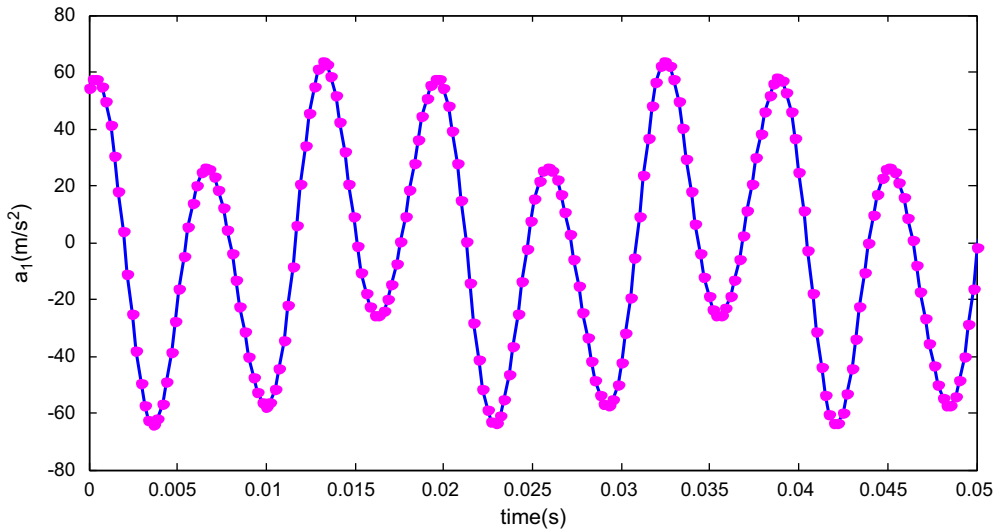


Fig. 5. Accelerations at the driving point, measured (solid line) and reconstructed (circles).

At this point, all prerequisites for calculation of the nonlinear restoring forces $S(t)$ and $N(t)$ are available and these restoring forces are constructed in the next section. Also a predictive model for friction force at the contact interface is proposed and its parameters are identified.

5. Identification of the contact restoring forces

A reduced discrete model of the system of order two is obtained using Galerkin projection introduced in Eq. (10) and the two nonlinear modes identified in Section 4. Force state mapping method is employed to solve these differential equations and subsequently the two contact forces, $S(t)$ and $N(t)$, are identified. In this study, experiments were performed at three different response levels. Table 2 tabulates the vibration amplitudes at these three loading cases and describes the amplitudes corresponding to two dominant harmonics of the acceleration signal at the deriving point. In this table, A_1 is the amplitude of acceleration signal first harmonic and A_2 is the amplitude of second harmonic.

Fig. 6 shows the identified force vs. displacement in each direction for the three different loading cases. The relative normal and tangential displacements, $\eta(t)$ and $\zeta(t)$, at the contact interface used in plotting Fig. 6 are described in Eqs. (11) and (12). The identified contact forces shown in Fig. 6 are expanded using Fourier series in the time domain up to fifth

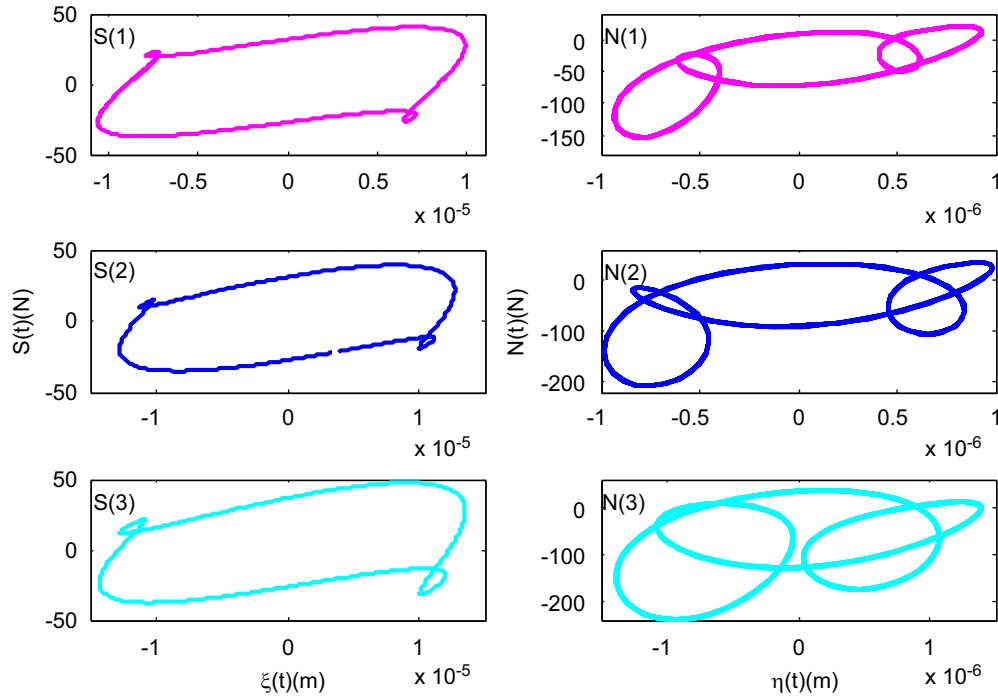


Fig. 6. Identified friction forces $S(i)$, and normal forces $N(i)$ at loading cases $i=1, 2, 3$.

harmonic as these harmonics appear in the generalized coordinates $q_1(t)$ and $q_2(t)$. In the three cases, all the nonlinear mechanisms were developed in the contact interface. The experimentally obtained hysteresis loops shown in Fig. 6 reveal the contact interface experienced micro/macro-slippage in the tangential direction and the micro-impacts were active in the normal direction. The variations of the identified normal force, $N(t)$, is always below the contact normal preload, 70 N, hence macro-impacts were not present in the contact interface. In addition, the normal stiffness hardening effect, due to the surface roughness, appears in the normal force–displacement plots of Fig. 6.

In this study, the identified friction forces are reconstructed using a new model based on a modified Valanis elasto-plastic constitutive model [3], which takes into account the effect of the variable normal force. The Valanis model relates the rate of change in the friction force to $\dot{\xi}(t)$ and $\dot{\zeta}(t)$ as

$$\dot{S}(t) = \frac{e_0 \dot{\zeta} \left[1 + (\lambda/e_0) \operatorname{sgn}(\dot{\zeta})(e_t \zeta - S(t)) \right]}{1 + \kappa (\lambda/e_0) \operatorname{sgn}(\dot{\zeta})(e_t \zeta - S(t))}, \quad \lambda = \frac{e_0}{\alpha_0 (1 - \kappa (e_t/e_0))}, \quad (21)$$

where its parameters are the contact shear stiffness in the stiction e_0 , contact tangential stiffness in macro-slippage e_t , a control parameter defining a smooth transition from stiction to macro-slippage which accounts for the micro-slips effect κ , and α_0 which sets the yield point in the hysteresis loop. A complete description of the Valanis model is provided in Refs. [3,7]. The Valanis model parameters are constant assuming the normal force applied to the contact interface is time invariant.

Thanks to the physical interpretation of the parameters in the Valanis model, the effects of micro-impacts on the friction forces can be implemented to the model by defining the interface parameters as a function of the contact normal force. First the parameter α_0 , representing the yield point in the hysteresis loop, is replaced by $\mu N(t)$ which allows the effect of normal load on the maximum friction force to be considered in the contact model. Next, the relationship between the normal load and contact shear stiffness is introduced to the model.

It is shown both mathematically and experimentally [21] that the contact shear stiffness, e_0 , is proportional to the contact area and dependent on the contact normal force. Based on the experimental observations an exponential relation is introduced in the present study, to account for the effect of normal force on the contact shear stiffness

$$e_0 = e_f \left(1 - e^{-(k_c N(t)/e_f)} \right) \quad (22)$$

The function described in Eq. (22), plotted in Fig. 7, has two parameters; the initial slop, k_c , and the ultimate stiffness, e_f , achieved by the joint interface at high normal preloads. The other two parameters of the contact model, *i.e.* e_t and κ , are regarded as independent of the contact normal preload. When the contact experiences macro-slip, regardless of the amount of normal load, the contact shear stiffness, e_t , is approximately zero; therefore, e_t is considered as a constant parameter. The parameter κ which controls the smooth transition from the stiction mode to macro-slippage is also

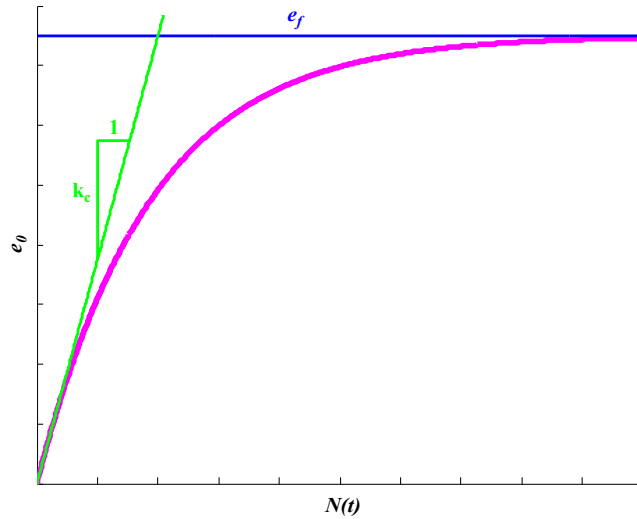


Fig. 7. Contact shear stiffness e_0 as a function of normal force $N(t)$.

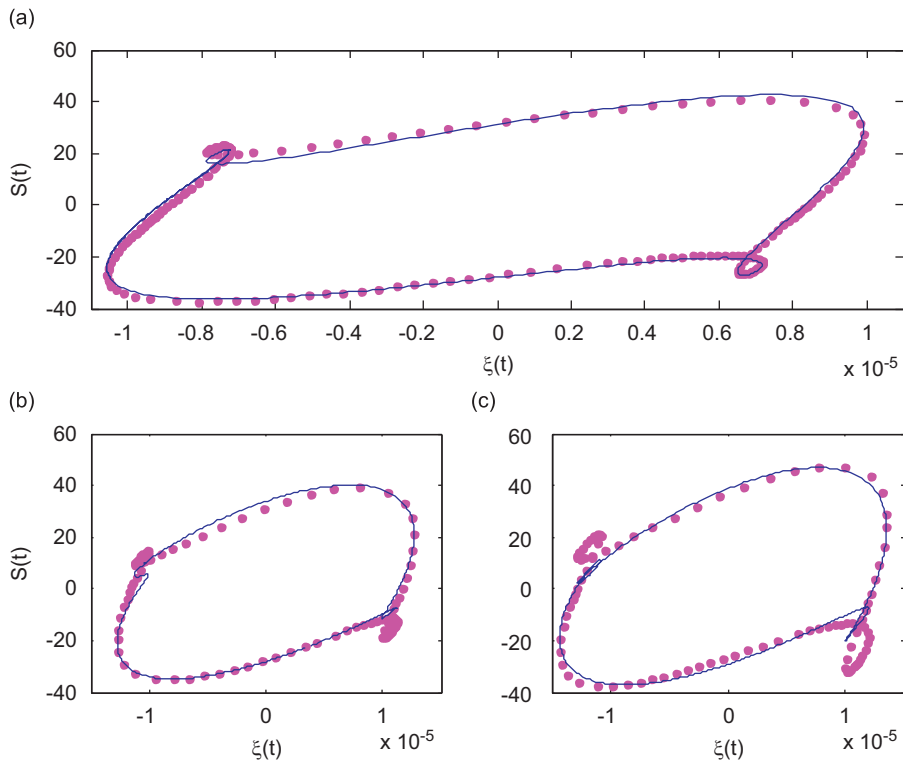


Fig. 8. The hysteresis loops $S(t)$ vs. $\xi(t)$, Measured (circles), predicted (solid line): (a) load case 1, (b) load case 2, and (c) load case 3.

considered a constant parameter in this study. Now, the contact model has been fully described and it is possible to compare the model predictions to the experimentally obtained results.

The first load case shown in Fig. 6, i.e. load case no. 1 in Table 2, is used to identify the friction model parameters e_f , k_c , e_t , κ and μ . An optimization procedure using Genetic Algorithm (GA) is performed to minimize the difference between the experimentally obtained friction forces and those predicted by the proposed model. The identified parameters are tabulated in Table 4.

Next, the identified model is used to regenerate the friction force in the two other load cases in order to validate the proposed contact model. Fig. 8 compares the hysteresis loops $S(t)$ vs. $\xi(t)$ obtained from experimental results with those predicted by the proposed model. The dependency of $S(t)$ to $\xi(t)$ is shown in Fig. 9 and where there is an excellent

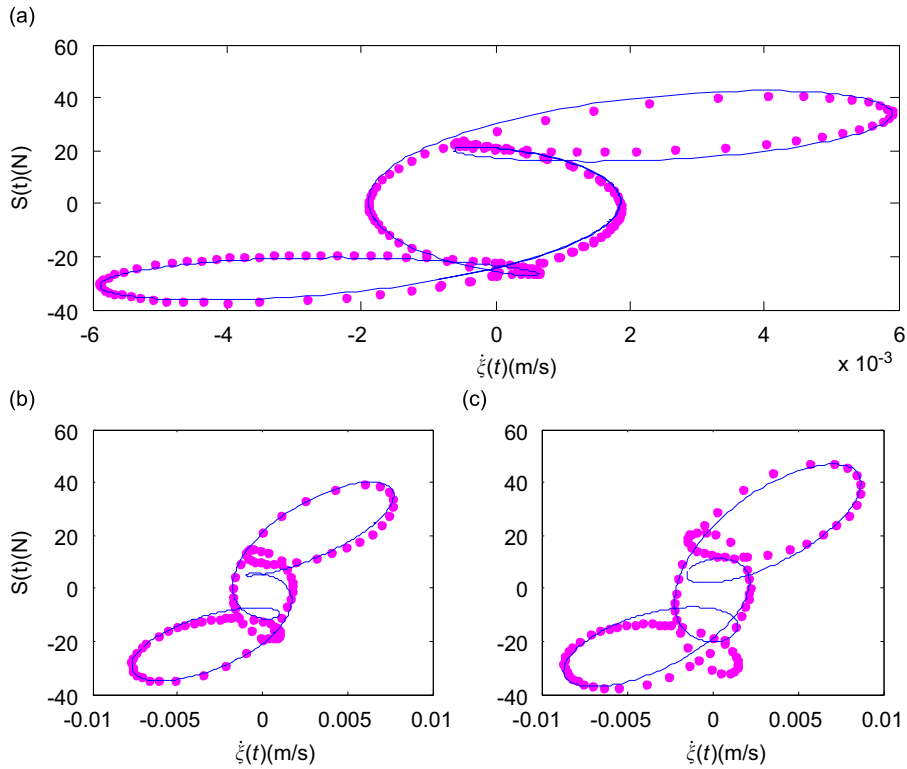


Fig. 9. The hysteresis loops $S(t)$ vs. $\dot{\xi}(t)$, Measured (circles), predicted (solid line): (a) load case 1, (b) load case 2, and (c) load case 3.

Table 4
The identified parameters of friction force model.

Parameter	Value
e_f (N/m)	3.857e7
k_c (1/m)	2.547e5
e_r (N/m)	≈ 0.0
κ	0.284
μ	0.397

agreement between the identified model predictions and the observed behavior of the frictional support. The time derivative $\dot{\xi}(t)$ is obtained using the periodicity property of $\xi(t)$, which consists of a small number of harmonics. The differentiation is performed in the frequency domain.

The internal loops of hysteresis curves in Figs. 8 and 9 are caused by strong presence of higher harmonics in the response with a single harmonic force excitation. Swevers et al. [6] have associated the internal loops with multiple jointing and disjoining of contact asperities during an excitation cycle. They have presented a physical model capable of predicting the internal loops observed in the measured data based on the jointing and disjoining of contact asperities concept. It is worth mentioning no gain of energy is observed in this model during multi-harmonic motion leading to internal loops. The same concept can be adopted here to explain the internal loops in the micro-vibro-impacts but more research work is needed to provide an analytical model similar to the one presented in Ref. [6].

The identified parameters are capable of modeling all the nonlinear mechanisms involved in the contact interface in load case one and show excellent agreement with experimental observations in two other load cases.

The proposed modifications to the Valanis model, made based on physical interpretations of the model parameters. These modifications enable the model to predict the frictional restoring forces of the contact interface accurately.

6. Conclusions

Dynamic characteristics of a beam with frictional contact support are investigated in situations where the main nonlinear mechanisms such as micro-impacts, stiction and slippage were developed in the contact interface. The first two natural frequencies of the test structure were designed to be near commensurable. The components of a dual sine

excitation force were tuned such that two independent nonlinear modes had considerable contributions in the response. The system response is expanded in this study using two nonlinear modes identified from the experimentally recorded data. Next, the Galerkin projection is carried out leading to a reduced order model of the system. The force state mapping method is performed using the reduced order discrete system and consequently, the unknown normal and frictional contact forces are obtained non-parametrically using the multimode identification procedure. A new friction model based on the Valanis elasto-plastic model is introduced, which takes into account the effect of micro-impacts on the contact friction force. The model parameters are identified using the experimentally obtained hysteresis loops. The proposed contact model is capable of regenerating frictional forces at other measured vibration levels, indicating the validity of the identified model in representing the physical mechanisms of the frictional support.

Appendix A

The extended Hamilton's principle is used to derive the governing equations of the system shown in Fig. 1:

$$\int_{t_1}^{t_2} (\delta T - \delta V + \delta W_{nc}) dt = 0, \quad (A1)$$

where T and V stand for the system kinetic and potential energy, respectively, and W_{nc} indicates the work done by non-conservative forces on the system. The kinetic energy is defined as

$$T = \frac{1}{2} \left(\int_0^L \rho A \left(\frac{\partial w(x,t)}{\partial t} \right)^2 dx + m_p \left(\frac{\partial w(L,t)}{\partial t} + r \frac{\partial^2 w(L,t)}{\partial t \partial x} \right)^2 + J_p \left(\frac{\partial^2 w(L,t)}{\partial t \partial x} \right)^2 + J_s \left(\frac{\partial \theta_s}{\partial t} \right)^2 \right) + \frac{1}{2} \left(m_s \left(\frac{\partial w(L,t)}{\partial t} + r \frac{\partial^2 w(L,t)}{\partial t \partial x} - \frac{\partial y_s}{\partial t} \right)^2 + m_s \left(\frac{\partial \xi}{\partial t} - 2r \frac{\partial^2 w(L,t)}{\partial t \partial x} + l_s \left(\frac{\partial \theta_s}{\partial t} \right) \right)^2 \right). \quad (A2)$$

The first term in the right hand side of Eq. (A2) refers to the beam kinetic energy due to its lateral vibrations. The next two terms describe the translational and rotational kinetic energies of the pin welded to the beam end. The pin has a lateral motion which is governed by the lateral deflection and rotation of the beam tip, due to offset r . The pin rotation is equal to the beam tip rotation. And the last three terms express the kinetic energy of the three degrees of freedom suspended mass block. The degrees of freedom are two in-plane translations and a rotation, θ_s . The potential energy is composed of four terms as follows:

$$V = \frac{1}{2} \left(\int_0^L EI \left(\frac{\partial^2 w(x,t)}{\partial x^2} \right)^2 dx + k_b u^2 + m_s g l_s \theta_s^2 + k_s y_s^2 \right), \quad (A3)$$

where the first term indicates the beam elastic potential energy. The second term stands for the potential energy due to the axial stretch in the beam. And the last two terms describe the potential energy in the string suspending the mass block.

The friction force, $S(t)$, and the contact normal force $N(t)$ are non-conservative and their effects are considered in the virtual work expression along with the external force applied at $x=d_p$,

$$\delta W_{nc} = S(t) \delta \xi(t) + N(t) \delta \eta(t) + \int_0^L f(t) \delta(x-d_p) \delta w(x,t) dx. \quad (A4)$$

Eqs. (A2)–(A4) are substituted in Eq. (A1), and after some manipulations and integration by parts one obtains

$$\int_{t_1}^{t_2} (\delta T - \delta V + \delta W_{nc}) dt = \int_{t_1}^{t_2} \left(- \int_0^L \left(EI \frac{\partial^4 w}{\partial x^4} + \rho A \frac{\partial^2 w}{\partial t^2} - f(t) \delta(x-d_p) + \left(S(t) + m_s \left(\ddot{\xi} - 2r \frac{\partial \ddot{w}(L,t)}{\partial x} + l_s \ddot{\theta}_s \right) \right) \frac{\partial^2 w}{\partial x^2} \right) \delta w(x,t) dx \right. \\ \left. + \left(EI \frac{\partial^3 w(L,t)}{\partial x^3} - m_p \ddot{\eta}(t) - m_s (\ddot{\eta}(t) - \ddot{y}_s) + N(t) + \frac{\partial w(L,t)}{\partial x} \left(S(t) + m_s \left(\ddot{\xi} - 2r \frac{\partial \ddot{w}(L,t)}{\partial x} + l_s \ddot{\theta}_s \right) \right) \right) \delta \eta(t) - \left(EI \frac{\partial^2 w(L,t)}{\partial x^2} + r EI \frac{\partial^3 w(L,t)}{\partial x^3} \right. \right. \\ \left. \left. + r S(t) \left(1 + \frac{\partial w(L,t)}{\partial x} \right) + J_p \frac{\partial \ddot{w}(L,t)}{\partial x} - r m_s \left(\ddot{\xi} - 2r \frac{\partial \ddot{w}(L,t)}{\partial x} + l_s \ddot{\theta}_s \right) \left(1 - \frac{\partial w(L,t)}{\partial x} \right) \right) \delta \left(\frac{\partial w(L,t)}{\partial x} \right) - \left(m_s \left(\ddot{\xi} - 2r \frac{\partial \ddot{w}(L,t)}{\partial x} + l_s \ddot{\theta}_s \right) \right. \right. \\ \left. \left. + k_b u + S(t) \right) \delta u - \left(J_s \ddot{\theta}_s + m_s l_s \left(\ddot{\xi} - 2r \frac{\partial \ddot{w}(L,t)}{\partial x} + l_s \ddot{\theta}_s \right) + m_s g l_s \theta_s \right) \delta \theta_s + (m_s (\ddot{\eta}(t) - \ddot{y}_s) - k_s y_s) \delta y_s \right) dt = 0. \quad (A5)$$

Separating the terms associated with variations of independent coordinates, Eqs. (1)–(7) are obtained. It should be noted the definitions for ξ and η used in Eq. (A5) is provided in Eqs. (8) and (9).

References

- [1] W.D. Iwan, A distributed-element model for hysteresis and its steady-state dynamic response, *ASME Journal of Applied Mechanics* 33 (1966) 893–900.
- [2] P.R. Dahl, Solid friction damping of mechanical vibrations, *AIAA Journal* 14 (1976) 1675–1682.
- [3] K.C. Valanis, A theory of visco-plasticity without a yield surface, *Archives of Mechanics* 23 (1971) 171–191.

- [4] Canudas de Wit, C.H. Olsson, K.J. Astrom, P. Lischinsky, A new model for control of systems with friction, *IEEE Transactions on Automatic Control* 40 (1995) 419–425.
- [5] V. Lampaert, J. Swevers, F. Al-Bender, Modification of the Leuven integrated friction model structure, *IEEE Transactions on Automatic Control* 47 (2002) 683–687.
- [6] J. Swevers, F. Al-Bender, C.G. Ganesman, T. Prajogo, An integrated friction model structure with improved pre-sliding behavior for accurate friction compensation, *IEEE Transactions on Automatic Control* 45 (2000) 675–686.
- [7] L. Gaul, J. Lenz, Nonlinear dynamics of structures assembled by bolted joints, *Acta Mechanica* 125 (1997) 169–181.
- [8] D.J. Segalman, Modeling joint friction in structural dynamics, *Structural Control and Health Monitoring* 13 (2006) 430–453.
- [9] S.W. Kim, Contact Dynamics and Force Control of Flexible Multi-Body Systems, PhD Thesis, Department of Mechanical Engineering, McGill University, Montreal, 1999.
- [10] K.H. Hunt, F.R.E. Crossley, Coefficient of restitution interpreted as damping in vibro-impact, *Journal of Applied Mechanics* 42 (1975) 440–445.
- [11] Y. Zhang, I. Sharf, Validation of nonlinear visco-elastic contact force models for low speed impact, *Journal of Applied Mechanics* 76 (2009). 051002-1–12.
- [12] I. Han, B.J. Gilmore, Multi-body impact motion with friction—analysis, simulation, and experimental validation, *Journal of Mechanical Design* 115 (1993) 412–422.
- [13] C.A. Tenaglia, D.E. Orin, R.A. LaFarge, C. Lewis, Toward development of generalized contact algorithm for polyhedral objects, *Proceedings of the 1999 IEEE International Conference on Robotics and Automation*, 1999, pp. 2887–2892.
- [14] Y. Gonthier, J. Mcphee, C. Lange, J.C. Piedbeuf, A regularized contact model with asymmetric damping and dwell-time dependent friction, *Multibody System Dynamics* 11 (2004) 209–233.
- [15] L. Gaul, M. Mayer, Modeling of contact interfaces in built-up structures by zero-thickness elements.
- [16] J.P. Den Hartog, Forced vibrations with combined Coulomb and viscous friction, *Transactions of the ASME: Applied Mechanics* 53 (1931) 107–115.
- [17] E.H. Dowell, Damping in beams and plates due to slipping at the support boundaries, *Journal of Sound and Vibration* 105 (1986) 243–253.
- [18] A.A. Ferri, Friction damping and isolation systems, *Journal of Mechanical Design* 117 (1995) 196–206.
- [19] E.J. Berger, Friction modeling for dynamic system simulation, *Applied Mechanics Reviews* 55 (2002) 535–577.
- [20] L. Gaul, R. Nitsche, The role of friction in mechanical joints, *Applied Mechanics Reviews* 52 (2001) 93–106.
- [21] W. Sextro, *Dynamical Contact Problems with Friction, Models, Methods, Experiments and Applications*, Springer-Verlag, Berlin, Heidelberg, 2007.
- [22] G. Gilardi, I. Sharf, Literature survey of contact dynamics modeling, *Mechanism and Machine Theory* 37 (2002) 1213–1239.
- [23] H. Ahmadian, H. Jalali, F. Pourahmadian, Nonlinear model identification of a frictional contact support, *Journal of Mechanical System and Signal Processing* 24 (2010) 2844–2854.
- [24] F. Pourahmadian, H. Ahmadian, H. Jalali, Identifying slip-slap forces in the contact interface using dual-mode excitation, *International Conference on Noise and Vibration Engineering (ISMA 2010)*, Leuven, Belgium, September 2010.
- [25] F. Pourahmadian, H. Jalali, H. Ahmadian, Identifying normal modes of a nonlinear system, *10th International Conference on Recent Advances in Structural Dynamics (RASD 2010)*, Southampton, UK, July 2010.
- [26] S.F. Masri, T.K. Caughey, A nonparametric identification technique for nonlinear dynamic problems, *Journal of Applied Mechanics* 46 (1979) 433–447.
- [27] A. Crawley, *Identification of nonlinear structural elements by force-state mapping* 24 (1986) 155–162/AIAA 24 (1986) 155–162.
- [28] K. Worden, G.R. Tomlinson, *Nonlinearity in Structural Dynamics: Detection, Identification and Modeling*, Institute of Physics Publishing, Bristol, Philadelphia, 2001.
- [29] W. Szemplinska-Stupnicka, The modified single mode method in the investigations of the resonant vibrations of nonlinear systems, *Journal of Sound and Vibration* 65 (1979) 475–489.
- [30] J. Bajkowski, W. Szemplinska-Stupnicka, Internal resonances effects—simulation versus analytical methods results, *Journal of Sound and Vibration* 104 (1986) 259–275.